ELSEVIER

Journal of Nuclear Materials 302 (2002) 125–134

journal of nuclear materials

www.elsevier.com/locate/jnucmat

An efficient model for the analysis of fission gas release

L.C. Bernard *, J.L. Jacoud, P. Vesco

Framatome ANP, 10 rue Juliette Récamier, 69456, Lyon cedex 06, France

Received 20 September 2001; accepted 29 January 2002

Abstract

This paper presents the fission gas release (FGR) model that has been developed at Framatome ANP and incorporated into its fuel rod performance code COPERNIC in order to accurately predict FGR into pressurized water reactor fuel rods under normal and off-normal operating conditions including UO_2, gadolinia and MOX fuels. The model is analytical, thus enabling fast and robust fuel rod calculations, a must within an industrial framework where safety evaluations may require the analyses of a full core and of a very large number of transients. Although the model is simple, it includes the most important FGR features: athermal, thermal, steady-state, and transient regimes, burst effect, rim formation, and MOX-type microstructure. The validation of the model covers 400 irradiated rods that include high burnups, high powers, short to long transients, and shows the quality of the prediction of the model in all types of conditions. As temperature is a key parameter that affects FGR, the COPERNIC thermal model is briefly described and its impact on fission gas released uncertainty is discussed. © 2002 Published by Elsevier Science B.V.

1. Introduction

Fission gas release (FGR) is a key phenomenon that must be assessed for fuel rod design and licensing. It contributes to the fuel rod internal pressure, with the associated risks of fuel thermal degradation and even clad failure. Therefore, all safety authorities require that the fuel internal pressure of each rod be limited by a pressure criterion. They typically ask that the gap between fuel and cladding does not reopen at high burnup, thus preventing a potential thermal feedback effect (where an increase of gap temperature may increase FGR, which, in turn, may increase the gap temperature). Moreover, for economical reasons, all electrical utilities are asking for light water reactor operation at ever-increasing burnup. The accurate prediction of FGR becomes more and more critical at high burnups because of several effects (gas production that is proportional to burnup, thermal degradation with burnup, fuel rim formation, etc.). Furthermore, MOX fuel (mixed oxide of plutonium and uranium) is one answer to reuse plutonium. MOX slightly enhances FGR, as compared to UO_2, and there is a need to better understand this effect.

Framatome ANP has developed a FGR model that takes into account the important physical phenomena. In an industrial framework, the model must also be efficient and in that context, it is kept as simple as possible. The FGR model is included into COPERNIC [1], the Framatome ANP advanced fuel rod performance code. COPERNIC accurately predicts steady-state and transient fuel performance at extended burnup. The code is based on the TRANSURANUS [2] code that provides fast, accurate, and numerically stable solutions. The Framatome ANP FGR model is also fast as it calculates the FGR fraction of an entire fuel rod history in less than 1 s on a workstation. This is most important for anticipated statistical studies (see for instance [3] and references therein, [4,5]) that require the analysis of a full fuel rod core. COPERNIC is validated on a large database obtained from many French and international programs. The qualification range extends to 67, 55, and 53 GWd/tM for UO_2, UO_2–Gd_2O_3, and MOX fuels, respectively.

---

* Corresponding author. Tel.: +33-4 72 74 72 94; fax: +33-4 72 74 88 33.

E-mail address: louis.bernard@framatome-anp.com (L.C. Bernard).

0022-3115/02/$ - see front matter © 2002 Published by Elsevier Science B.V.
PII: S0022-3115(02)00793-6

The COPERNIC thermal model was upgraded [1,6] as recent high and ultra-high burnup data became available [7–10]. The FGR model had to be upgraded as FGR strongly depends on fuel temperature. With recent MOX data, it was also possible to take into account the type of MOX fuel microstructure in the FGR model. Section 2 briefly describes the thermal model and its qualification. The following sections detail the FGR modeling: athermal regime and rim formation, thermal regime under separate and combined steady-state and transient operation, burst effect, mixed oxide effects (MOX and gadolinia fuels), and validation on experimental data.

2. Thermal model

Temperature is a key parameter that affects FGR. Therefore, accurate prediction of temperature is a prerequisite for good FGR modeling. Many factors contribute to the fuel temperature distribution, like corrosion, mechanical and thermal gaps, gap closure and reopening, radial power distribution, rim formation, etc. The accurate determination of the degradation of the fuel thermal conductivity with burnup remains essential. There is still a need for further progress. The Lucuta et al. [11] and the HALDEN [8] relationships for fuel thermal conductivity have been widely used, but they predict somewhat different fuel conductivity degradation with burnup, as shown on Fig. 1.

A simple relationship that matches well a large database was developed for the COPERNIC code [1,6]. This relationship has the form

$$\lambda_{100\%} = (A_1 + A_2 T + A_3 B + A_4 f(T))^{-1} + g(T), \qquad (1)$$

where $\lambda_{100\%}$ (W/m/K) is the 100% dense fuel conductivity, B is burnup, and T is temperature. The terms with the parameters A_1 and A_2 represent the phonon contribution for unirradiated materials. The term with parameter A_3 (>0) represents the degradation of the thermal conductivity with burnup for irradiated materials. The function $f(T)$ is the radiation damage term derived by Lucuta et al. [11] that is important at low temperatures and $g(T)$ represents the electronic conductivity. The expressions for MOX and UO_2 fuels differ only by the values of the parameters A_1 and A_2 (the complete description of the thermal model is outside the scope of this paper). The values used for stoichiometric UO_2 fuel are $A_1 = 0.0375$ m K/W, $A_2 = 2.165 \times 10^{-4}$ m/W, $A_3 = 1.70 \times 10^{-3}$ m K/W/(GWd/tM), and $A_4 = 0.058$ m K/W, and the functions f and g read

$$f(T) = \left[1 + \exp\left(\frac{T - 900}{80}\right)\right]^{-1},$$

$$g(T) = 4.715 \times 10^9 T^{-2} \exp\left(-\frac{16361}{T}\right). \qquad (2)$$

Fig. 2 shows that the COPERNIC and the Lucuta et al. relationships are quite close. Overall, the COPERNIC relationship predicts a slightly higher degradation with burnup.

The Framatome ANP database for the validation of the COPERNIC thermal model is summarized on Table 1. The data were obtained in the French test reactors OSIRIS and SILOE run by the Commissariat à l'Energie Atomique (CEA) and in the test reactor HALDEN run by the Organisation for Economic Co-operation and Development (OECD). The experiments EXTRAFORT [7] and IFA-562.2-16 [8] (UO_2 fuels), FIGARO [9] (MOX fuel), and IFA-515.10-2 [12] (gadolinia fuel) are particularly representative of high burnups and relatively high powers and are highlighted in Table 1.

The measured fuel centerline temperatures above linear heat generation rates (LHGR) of 10 kW/m have

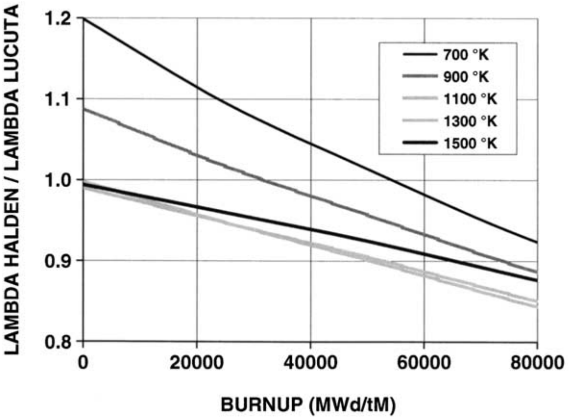

Fig. 1. Comparison between the UO_2 pellet thermal conductivity of HALDEN [8] and of Lucuta et al. [11].

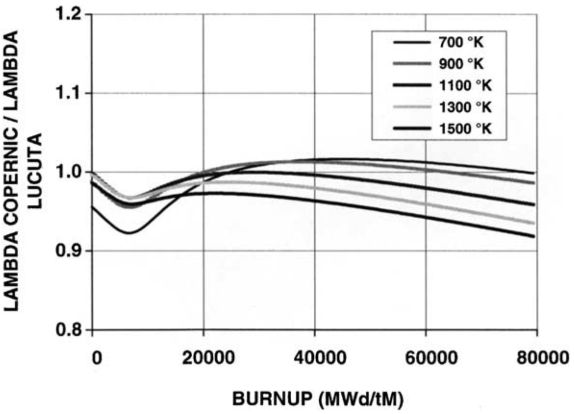

Fig. 2. Comparison between the UO_2 pellet thermal conductivity of COPERNIC [1] and of Lucuta et al. [11].

Table 1
Framatome ANP database for the validation of the COPERNIC thermal model (burnup and power ranges are for the temperature centerline measurements). The high power, high burnup cases are in italic

Experiment	Fuel	Sponsor	Reactor	Burnup range (GWd/tM)	LHGR range (kW/m)
CONTACTB	UO_2	CEA	SILOE	0–*9.5*	0–*26*
BOSS	UO_2	CEA	OSIRIS	0–*0.6*	0–*60*
GRIMOX 01	UO_2	CEA	SILOE	0–0.7	0–*24*
GRIMOX 02	UO_2	CEA	SILOE	0–4.7	0–*37*
GDGRIF 1	UO_2	CEA	SILOE	0–3.5	0–*32*
EXTRAFORT	*UO_2*	*CEA*	*OSIRIS*	*64*	*0–31*
GRIMOX 01	MOX	CEA	SILOE	0–0.7	0–*26*
GRIMOX 02	MOX	CEA	SILOE	0–4.7	0–*39*
GDGRIF 1	UO_2–Gd_2O_3	CEA	SILOE	0–*2.1*	0–*24*
GDGRIF 2	UO_2–Gd_2O_3	CEA	SILOE	0–6.6	0–*35*
IFA 431-1	UO_2	OECD	HALDEN	0–*5.3*	0–*35*
IFA 431 -3	UO_2	OECD	HALDEN	0–*5.7*	0–39
IFA 432-1	UO_2	OECD	HALDEN	0–*10*	0–*46*
IFA 432-3	UO_2	OECD	HALDEN	0–*43*	0–*47*
IFA 513-1	UO_2	OECD	HALDEN	0–*12*	0–*47*
IFA 513-2	UO_2	OECD	HALDEN	0–*6*	0–*34*
IFA 513-6	UO_2	OECD	HALDEN	0–*11*	0–*47*
IFA 515.10-1	UO_2	OECD	HALDEN	0–58	0–*23.4*
IFA 562.2-16	*UO_2*	*OECD*	*HALDEN*	*0–102*	*0–38*
IFA 562.2-18	UO_2	OECD	HALDEN	0–*57*	0–*39*
IFA 606 (FIGARO)	*MOX*	*OECD*	*HALDEN*	*50*	*0–32*
IFA 610.2	MOX	OECD	HALDEN	*59*	0–15
IFA 515.10-2	*UO_2–Gd_2O_3*	*OECD*	*HALDEN*	*0–64*	*0–23.9*

been retained to validate the COPERNIC thermal model. Overall, there are 3425 such measurements (918 values for the CEA experiments and 2507 for the HALDEN experiments). The mean of the ratios (M/P) of the measured values over the predicted values is shown on Table 2 for three classes of data (above 10, 20, and 30 kW/m). There is no bias with respect to the power level.

The quality of the COPERNIC predictions is good for all the subsets of Table 2. The uncertainty of the COPERNIC thermal model can be inferred without any assumption on the shape of the data distribution by using the binomial distribution. As a result, the thermal uncertainty is comparable to the state-of-the-art modeling [13] as it is below 10% at a 95% level with a confidence level of 95%.

Table 2
Quality of the prediction of the COPERNIC thermal model for different ranges of power level

Ratio of measured-to-predicted temperatures (kW/m)	Mean	Standard deviation	Number of points
LHGRs $>$ 10	1.002	0.042	3425
LHGRs $>$ 20	0.995	0.049	1617
LHGRs $>$ 30	0.98	0.054	440

3. Athermal and rim FGR models

The COPERNIC FGR model takes into account athermal and thermally activated mechanisms. Athermal release is produced through recoil and knockout mechanisms. Neglecting the recoil contribution, the athermal FGR fraction is of the form [14] $C_1(S/V)B$ where, after best fitting our database, the model parameter $C_1 = 1.3 \times 10^{-7}$ cm/(GWd/tM), S/V is the specific surface of the fuel (cm^{-1}) and B is burnup (GWd/tM). Contributions from fuel open porosity and from the rim are included in the specific surface

$$S/V = (S/V)_0 + C_2 p_{\text{open}} + (S/V)_{\text{rim}}, \tag{3}$$

where $(S/V)_0$ is the intrinsic specific surface, the model parameter $C_2 = 50\,000$ cm^{-1}, p_{open} is the open porosity (fraction), and $(S/V)_{\text{rim}}$ is the additional specific surface that develops in the rim region at high burnup. Indeed, typical features of the rim microstructure include a subdivision of the grains and an increase of the porosity. Both effects contribute to an increase of the specific surface.

A simple fuel rim model has been implemented that has the form

$$w = \text{Max}[0; C_3(B_S - 70); C_4(B_A - 45)], \tag{4}$$

where w (mm) is the width of the rim, B_S and B_A are the pellet surface and pellet averaged burnups (in GWd/tM), respectively, and the model parameters $C_3 = 4 \times 10^{-3}$ mm/(GWd/tM) and $C_4 = 8 \times 10^{-3}$ mm/(GWd/tM). Eq. (5) translates the experimental observation that a specific rim microstructure develops whenever the burnup exceeds a high threshold value. Two threshold values are used for the only purpose of taking into account different radial burnup profiles inside the pellet. The rim width is either adjusted on the pellet surface burnup or on the pellet average burnup depending of the value of the burnup ratio $\mathrm{BR} = B_S/B_A$, at it is illustrated on Fig. 3(a). Inside the rim, the specific surface takes the form

$$(S/V)_{\mathrm{rim}} = C_5(r - r_S + w),$$
$$0 < (S/V)_{\mathrm{rim}} < 5000\ \mathrm{cm}^{-1}, \qquad (5)$$

where r is the radial distance to the pellet center, r_S is the pellet radius, and $C_5 = 75\,000\ \mathrm{cm}^{-1}\,\mathrm{mm}^{-1}$ is a model parameter based upon experimental data. The evolution of the rim specific surface inside the rim region is illustrated on Fig. 3(b).

The athermal model parameters were adjusted on the experimental data shown on Fig. 4 that were obtained for fuel rods irradiated in pressurized water reactors (PWRs) run by the French utility Electricité de France (EDF). Released fractions from PWR Framatome ANP fuels (that have a negligible open porosity) are plotted vs. burnup. There are clearly two distinct regions, at low and high burnup. At low burnup, there are no rim and no thermal FGR. Then, FGR is proportional to burnup and the coefficient C_1 is adjusted to fit the data. At high burnup, additional fission gas can be released from either a thermal effect or a rim effect or both. We separate out both effects by observing fuel pellet micrographs. We adjust the rim parameters on the data that do not show a radius of inter-granular bubble precipitation (signature of thermal release).

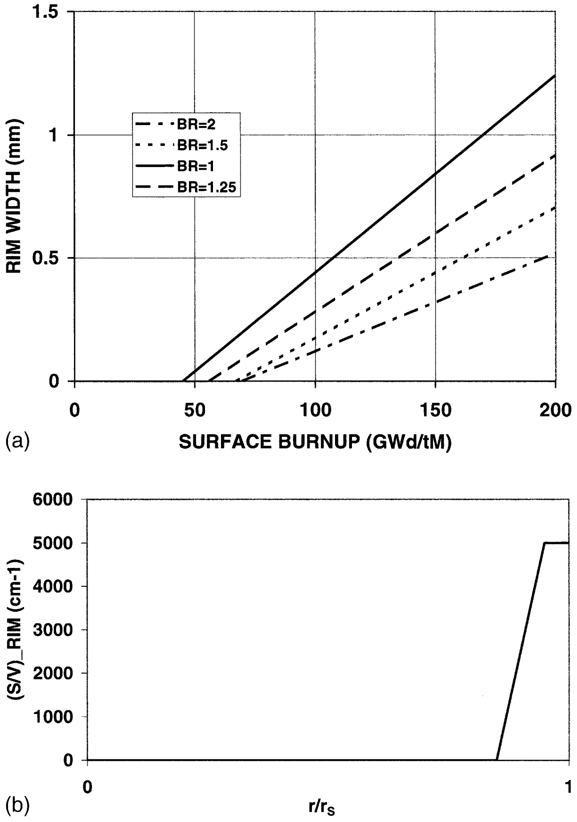

Fig. 3. (a) Evolution of the rim width with burnup; BR is the ratio of the surface burnup to the average burnup. (b) Evolution of the specific surface inside the rim.

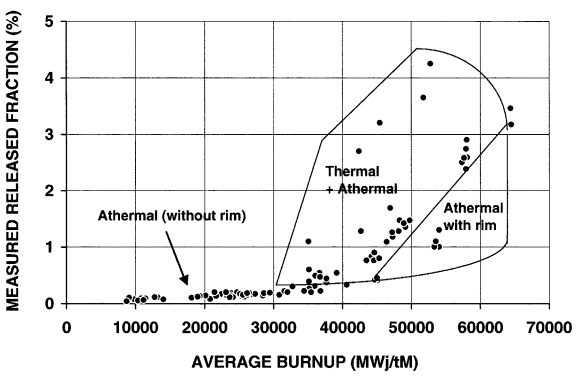

Fig. 4. Gas release fractions from Framatome ANP fuel rods irradiated in EDF reactors.

4. Thermal FGR model

4.1. Background

The thermal FGR model is based on previous closely related models [15–17]. Thermal FGR follows a two-stage diffusion process. First, the gas atoms diffuse from inside the grain to the grain boundaries where they accumulate until a saturation (incubation) threshold is reached. Gas atoms are brought back into solution inside the grain from the grain boundary by fission spikes and within a thin layer at the grain boundary. This irradiation-induced resolution counteracts the diffusion flux and delays the onset of release. This onset occurs when the grain boundary concentration exceeds the saturation threshold. We suppose instant release above threshold, neglecting all the phenomena that bring the atoms from grain boundary to the fuel rod free volumes like percolation, tunnel formation, diffusion along grain faces and tunnels and fuel column, etc. All these phenomena contribute to the kinetics of the release but may not affect much the total inventory of gas release.

The problem is then to solve a diffusion equation inside the grain with a time-varying condition at the grain boundary. Idealizing the grain by a sphere of radius a, the diffusion equation reads in one-dimensional spherical geometry

$$\frac{\partial c}{\partial t} = \beta + \nabla(D\overrightarrow{\nabla c}), \tag{6}$$

where $c(u,t)$ is the local gas concentration, u and t are the space and time variables, β is the creation rate and D is the diffusion coefficient. Following [17], the boundary condition is given by

$$c(a,t) = \frac{bN\delta}{2D}, \tag{7}$$

where b is the probability of the resolution of the inter-granular atoms, N is the surface density (number of atoms per unit area) at the grain boundaries, and δ is the width of the inter-granular resolution layer. Gas balance equations within grain and at grain boundary close the problem. When the surface density is lower than the saturation density, N_S, the balance equation reads

$$\int c\,\mathrm{d}v + \frac{3N}{2a} = \int \mathrm{d}t \int \beta\,\mathrm{d}v, \tag{8}$$

where integrals are integrated in time and space (over the grain volume, dv being the differential volume). Above saturation, the release fraction, F, is obtained from the relation

$$F = 1 - \left[\int c\,\mathrm{d}v + \frac{3N_S}{2a}\right] \Big/ \int \mathrm{d}t \int \beta\,\mathrm{d}v. \tag{9}$$

The set of Eqs. (6)–(9) forms a mathematically well-posed problem, although non-trivial to solve numerically in an efficient way. Ref. [17] presents a fast and accurate algorithm that is based on the finite volume method for space integration and on a two-step time integration. This algorithm proved to yield good predictions for our whole gas release database but for of a few cases. Once integrated in a fuel rod computer code, the algorithm needs, for improved accuracy, to solve the problem for two time-steps. The first time-step is imposed by the code according to multiple criteria involving power history inputs and the accuracy of other fuel rod models and the second time-step gives optimal accuracy for the FGR model numerical algorithm. When these two time-steps differ two much, there is a loss of accuracy. Also, the iteration scheme to solve the balance Eq. (8) may slow down. To circumvent these difficulties and to reach a model that is 100% robust, semi-analytical approximations to the above-mentioned problem were sought for. Excellent simple approximations are found and are described in next subsections.

4.2. Incubation threshold approximation

First, we detail the expression of the diffusion coefficient, D. We use the diffusion coefficient of Turnbull's et al. [18] which is the sum of three components D_1, D_2, and D_3. The D_1 term represents the intrinsic diffusion in the absence of irradiation. The D_2 and D_3 terms represent the thermal and athermal contributions induced by irradiation. The presence of D_3 has been recently open to question [19]. However, it is natural to consider such a term as representing the physical process of fuel atoms being knocked out of equilibrium location by fission spikes and randomly returning back in place. This process is equivalent to diffusion and should be independent or weakly dependent upon fuel temperature. One could also view D_3 as representing a physical continuity between the athermal and the thermal FGR regimes. The final form of the diffusion coefficient, D, is chosen as follows:

$$\begin{aligned} D_1 &= D_{01}\exp\left(-\frac{T_{01}}{T}\right), \\ D_2 &= D_{02}\exp\left(-\frac{T_{02}}{T}\right)\sqrt{\frac{P'f_R}{20}}, \\ D_3 &= D_{03}\frac{P'f_R}{20}, \\ D &= \left[\frac{1}{D_1+D_2+D_3} + \frac{1}{L^2b'}\right]^{-1}, \end{aligned} \tag{10}$$

where T is the local temperature (K), P' is the LHGR (kW/m), f_R is the radial power factor (ratio of local to pellet average volumetric power values), $D_{01} = 7.6 \times 10^{-10}$ m^2/s, $T_{01} = 35000$, $D_{02} = 1.77 \times 10^{-15}$ m^2/s, $T_{02} = 13800$, and $D_{02} = 2 \times 10^{-21}$ m^2/s. In Eq. (10), a correction is added due to the irradiation-induced resolution of intra-granular bubbles, following [20]. The product L^2b' is chosen equal to 10^{-15} m^2/s where L is the mean free path between two intra-granular bubbles and b' is the probability of resolution of intra-granular atoms by fission spikes.

As shown in [17], the solution of the set of Eqs. (6)–(9) matches well the experimental incubation threshold. An analytical approximation of this solution is found following [15] and [17]. The evolution of the surface density at the grain boundary follows approximately the equation [15]

$$\frac{\mathrm{d}N}{\mathrm{d}t} = 4\beta\sqrt{\frac{Dt}{\pi}}\left(1 - \frac{Nb\delta}{2D\beta t}\right). \tag{11}$$

The incubation time, t_I, is given by the solution of the previous equation for $t_I = t(N_S)$ where N_S is the threshold value of the surface density. Two approximate asymptotic solutions of this equation are found [17] for the incubation burnup, B_I. At low temperatures

$$B_I \sim \frac{bN_S\delta}{2(D_2+D_3)} \tag{12}$$

and at high temperatures

$$B_I \sim \left[\frac{9N_S^2\beta}{8\pi}\left(\frac{1}{D_1}+L^2b'\right)\right]^{1/3}. \tag{13}$$

Two important remarks enable one to combine these two last expressions in one single expression. First, $T_{02} \sim T_{01}/3$ and therefore $\exp(-T_{01}/T)^{1/3} \sim \exp(-T_{02}/T)$. Second, there are great uncertainties on the values of the microscale parameters (b, δ, and N_S) and, a fortiori, on the combination of these parameters. We therefore seek a solution for the incubation threshold of the form

$$B_I = \frac{B_1}{\exp\left(-\frac{T_{02}}{T}\right)+\frac{(T-T_1)}{T_2}} + B_2, \tag{14}$$

where B_I is the incubation burnup at temperature T (K) and $B_1 = 0.0012$ GWd/tM, $B_2 = 2.5$ GWd/tM, $T_1 = 603$, and $T_2 = 1.59 \times 10^7$ are model parameters adjusted on our FGR experimental database. This expression is represented on Fig. 5 (solid curve) and can be viewed as a generalization of the HALDEN threshold [21]. Indeed, the form of the HALDEN threshold is obtained if one neglects the term B_2 and the term involving T_1 and T_2. One may notice that, towards high burnup values, the value of the HALDEN threshold temperature is higher than the temperature given by expression (14). In one hand the HALDEN threshold temperature is quoted for 1% release and expression (14) is for 0% thermal release. On the other hand, the HALDEN threshold was derived for data below 30 GWd/tM and recent HALDEN data above 50 GWd/tM show 1% release for temperatures below the initial HALDEN temperatures.

Fig. 5 shows that expression (14) is an excellent approximation to the numerical solution (solid points) that is obtained by using the method described in [17] for solving the set of Eqs. (6)–(9). The following values are used for the numerical solution: b (s^{-1}) $= 3 \times 10^{-6}$ $(P'/20)$, $\delta = 8 \times 10^{-8}$ m, and $N_S = 10^{20}$ m^{-2}. The dashed curves are for MOX fuels and are explained later in Sections 5 and 6.

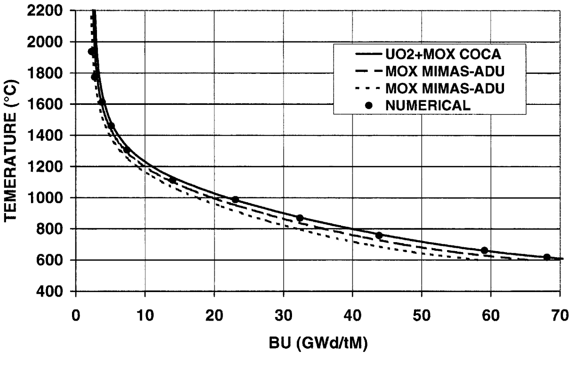

Fig. 5. FGR model: incubation threshold.

4.3. Steady-state approximation

We find a second simple analytical approximation to the solution of Eqs. (6)–(9) for finite release above threshold conditions ($t > t_I$) in the special case when the diffusion coefficient D is constant with time, that is, in steady-state conditions. This approximation reads [15] in terms of the release fraction, F_{SS},

$$F_{SS} = \left(1-\frac{t_I}{t}\right)F_1(\tau) + \left(1-\frac{3N_S}{2a}-\frac{bN_S\delta}{2D\beta t_I}\right)\frac{t_I}{t}F_2(\tau), \tag{15}$$

where F_1 and F_2 are the Booth [22] solutions

$$F_1(\tau) = 1-\frac{6}{\tau}\sum_{n=1}^{\infty}\frac{1-\exp(n^2\pi^2\tau)}{n^4\pi^4}, \qquad F_2(\tau) = 1-6\sum_{n=1}^{\infty}\frac{\exp(-n^2\pi^2\tau)}{n^2\pi^2}, \tag{16}$$

evaluated at the reduced time $\tau = D(t-t_I)/a^2$. Eq. (15) is further simplified by taking notice that, in Eq. (15), the term with F_2 is almost always negligible as compared to the term with F_1. Therefore, the expression of the fractional release value is simplified by neglecting the term with F_2 in the expression (15). Also, F_1 is simply evaluated with the Booth [22] asymptotic expansions

$$\tau \leqslant 0.1, \quad F_1 = 4\sqrt{\frac{\tau}{\pi}}-\frac{3\tau}{2}, \qquad \tau > 0.1, \quad F_1 = 1-\frac{1}{15\tau}\left(1-\frac{90}{\pi^4}\exp(-\pi^2\tau)\right). \tag{17}$$

The merit of the above approximations will be assessed later in Section 6 that describes the validation of the FGR model on experimental results.

4.4. Transient and burst effect approximations

Transient is meant as a power increase during a power ramp. The evolution of the grain gas concentration is modeled, in part, by the same diffusion process as in the steady-state case and, in addition, by a burst effect. This burst effect is a consequence of complex processes, like the coalescence of inter-granular bubbles, tunnel opening, etc., that vent out part of the grain boundary gas.

Diffusion is described by the solution of the diffusion equation when the creation term βt is negligible with respect to the diffusion term (this hypothesis is valid for typical short transients)

$$F_{TR}(\omega) = 1-6\sum_{n=1}^{\infty}\frac{\exp(-n^2\pi^2\omega)}{n^2\pi^2}, \tag{18}$$

where F_{TR} is the released fraction due to diffusion for a transient starting at time t_0 and $\omega = \int_{t_0}(D\,\mathrm{d}t/a^2)$.

Again, Eq. (18) is efficiently calculated with the Booth [22] asymptotic expansions

$$\begin{aligned} &\omega \leqslant 0.1, \quad F_{\mathrm{TR}} = 6\sqrt{\frac{\omega}{\pi}} - 3\omega, \\ &\omega > 0.1, \quad F_{\mathrm{TR}} = 1 - \frac{6}{\pi^2}\exp(-\pi^2\omega). \end{aligned} \tag{19}$$

The burst term, due to the complexity of phenomena involved, is empirical and is simply modeled by an exponential decay of the grain boundary concentration with a relaxation time that is proportional to the diffusion coefficient. We require of course that the value of the concentration during transient be bounded by the value, c_{SS}, that the concentration would have for a steady-state at peak transient power and starting at zero time. In summary, the total gas concentration during a transient is expressed as follows:

$$\begin{aligned} c = \mathrm{Max}\Bigg(& c_0[1 - F_{\mathrm{TR}}(t - t_0)] \\ & - c_{B0}\exp\left(-\frac{D}{a^2}\frac{t - t_0}{C_6}\right); c_{\mathrm{SS}}\Bigg). \end{aligned} \tag{20}$$

In Eq. (20), c_0 is the total concentration at time t_0 (including both intra- and inter-granular contribution), and c_{B0} is the inter-granular concentration at time t_0. c_0 and c_{B0} are the result of code calculations until time t_0. These calculations are usually done for time-varying conditions and are divided into a succession of steady-state and transient regimes where the above approximations apply. The previous approximations show how to calculate the total concentration. It remains to derive an approximation for the evolution of the inter-granular concentration $c_B(t)$. During steady-state, $c_B(t)$ is approximately a solution of Eq. (11). The asymptotic expansion of this solution [15] for large times (but before incubation) shows that, during steady-state, $c_B(t)$ is proportional to time t. We assume this dependence and the comparison with the numerical solution of the set of Eqs. (6)–(9) shows that it is a reasonable approximation on average. At or above incubation and during steady-state, $c_B = 3N_{\mathrm{S}}/(2a)$. During transient, c_B is assumed to decay exponentially with time according to Eq. (20) where $C_6 = 0.05\ \mathrm{s}^{-1}$ is a model parameter adjusted to fit burst data. To complete the calculation of the FGR evolution, one needs an algorithm that switches from one regime to another regime. This is the object of Section 4.5.

4.5. Combined steady-state and transient approximation

In the general case when time-varying conditions apply, an algorithm is needed to switch from the steady-state model to the transient model back and forth. The switch is tested at each time-step Δt and is based upon the parameter R defined as

$$R = \frac{c - c_{\mathrm{SS}}}{\beta\Delta t}. \tag{21}$$

In expression (21), c is the concentration that is the result of calculations up to the beginning of the time-step, t. c_{SS} is the concentration calculated at time t with the steady-state model but at the new conditions of power and temperatures defined at the end of the time-step $t + \Delta t$. When R is small, the power change is quasi-steady and the steady-state model applies directly. Otherwise, $R > 0$ reflects a fast-rising power change and the transient model applies, while $R < 0$ reflects a decreasing power change and the steady-state model applies but using an equivalent time ('concentration-hardening' solution).

Fig. 6 illustrates the evolution of the concentration of fission product gases for a zoom in burnup typical of an irradiation when conditions change from a steady-state condition (at power level P_1) to a transient condition (at power level P_2) and back (at power level P_1). The algorithm is basically the same for the evolution of the total concentration (c) and for the inter-granular concentration (c_B). Both concentrations increase until the incubation burnup B_{I} (the total concentration, then, is equal to the gas creation as there is no gas release, and the inter-granular concentration is linear as mentioned in Section 4.4). During the first steady-state, i.e. between burnups B_1 and B_2, c_1 follows the steady-state approximation described in Section 4.3. c_{B1} remains constant as we simply take N_{S} as a constant (the model could be later refined by choosing an equation of state for N_{S} involving for instance the evolution of gas pressure inside the inter-granular bubbles). During the transient, i.e. between burnup B_1 and B_2, c_1 and c_{B2} follow the approximation described in Section 4.4. During the second steady-state, i.e. for B greater than B_2, c_3 and c_{B3} are evaluated at equivalent burnups, B_{E} and B_{EB}, such that $c_3(B) = c_1(B_{\mathrm{E}})$ and $c_{B3}(B) = c_{B1}(B_{\mathrm{EB}})$. For an entire full rod irradiation, there are usually many power

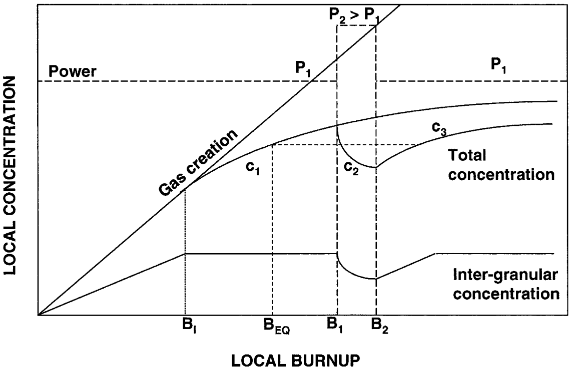

Fig. 6. General algorithm to switch from FGR steady-state to transient and back.

changes and the algorithm proves robust enough to handle as many power changes as needed to represent the fuel rod power histories.

5. Mixed oxides

The model was extended to MOX and gadolinia fuels. MOX fuels have different microstructure according to the manufacturing process. Framatome ANP uses the MIMAS process (MIcromized MASter blend) where a secondary blend adds UO_2 to a primary blend of UO_2 and PuO_2. Both ammonium uranyl carbonate (AUC) and ammonium diuranate (ADU) conversion processes are used. MOX MIMAS fuels have a heterogeneous microstructure with Pu-rich agglomerates where the local burnup is high. MIMAS-ADU fuels tend to be more homogeneous than MIMAS-AUC fuels. CEA used the COCA (CO-milling CAdarache) process that produces a MOX homogeneous structure. As FGR is typically a non-linear increasing function of burnup, the volume averaged FGR for MOX MIMAS fuels must be higher that the FGR for the average burnup. This effect is modeled by using an incubation burnup that can be lower for MOX fuels than for UO_2 fuels, depending upon the degree of heterogeneity of the MOX microstructure. This translates into a simple expression

$$(B_\mathrm{I})_\mathrm{MOX} = C_7(B_\mathrm{I})_{\mathrm{UO}_2}, \tag{22}$$

where the model parameter C_7 is fitted on experimental data (see Section 6). Eq. (22) means that, for MOX fuels, expression (14) holds where parameters B_1 and B_2 are now replaced by C_7B_1 and C_7B_2. C_7 should be equal to 1 for COCA MOX fuels that are homogeneous (then the threshold curve should the same as for UO_2) and C_7 should be less for MOX MIMAS fuels. The ADU-type proves to be more homogeneous than the AUC-type and therefore, C_7 should be higher for ADU than for AUC.

The temperature of the gadolinia fuel is higher because the thermal conductivity is less than that of UO_2 fuels. However, the observed releases from these types of oxide are comparable. The temperature effect is offset by a decrease in the diffusion coefficient with increasing quantities of gadolinium. This effect is simply modeled by decreasing the temperature used in the FGR model by an amount that is proportional to gadolinium content.

6. FGR model validation

The Framatome ANP steady-state FGR database includes more than 290 fuel rods irradiated in commercial or experimental reactors with rod average burnups up to 67 GWd/tM. The comparison of the measured and predicted FGR for steady-state irradiation is shown in Fig. 7. The quality of the prediction of the FGR model can be deduced from these results. Fig. 8 shows the upper-bound uncertainty limit of the model at the 95% level. This limit is close to 40% (in absolute values) above the best-estimate predictions in the range of release fractions below 10% that is typical of PWR operation. Above 10%, the uncertainty decreases. Temperature uncertainty is an important part of FGR uncertainty. For example, at normal PWR operation (typically 1000 °C), D_2 is the main component of diffusion, τ is small, and F is about proportional to $D_2^{0.5}$ from Eqs. (15) and (17). A 5% uncertainty on the temperature level could lead to a 30% uncertainty on the FGR as a result of the value of the activation energy $T_{02} = 13\,800$ K.

Fig. 9 details the validation of the MOX model according to fuel microstructure. The best fit to the data shown on Fig. 9 is obtained with $C_7 = 1$ for COCA, $C_7 = 0.9$ for ADU, and $C_7 = 0.8$ for AUC. The trend with the homogeneity of the MOX microstructure follows what is expected from the above discussion. The incubation threshold is show on Fig. 5 for the three values of C_7 (1, 0.9, and 0.8). Fig. 10 compares predic-

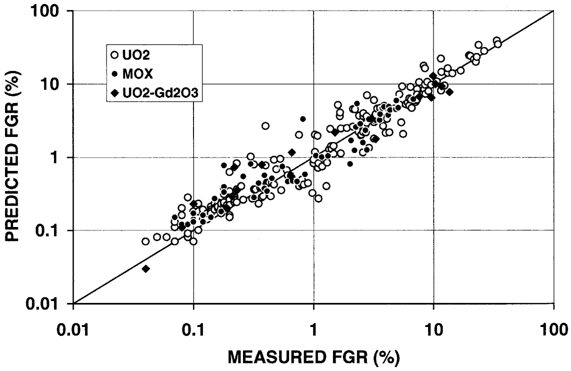

Fig. 7. Validation of the FGR steady-state model.

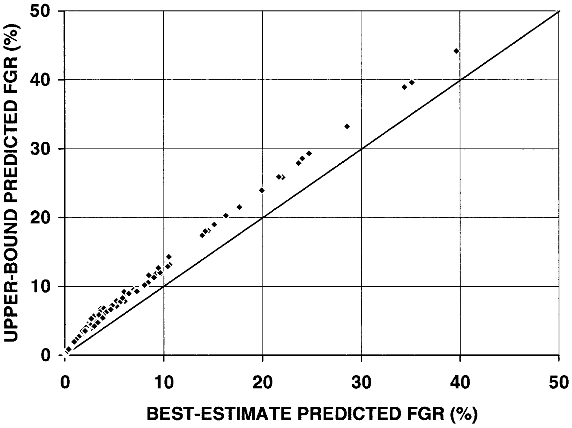

Fig. 8. FGR steady-state model uncertainty.

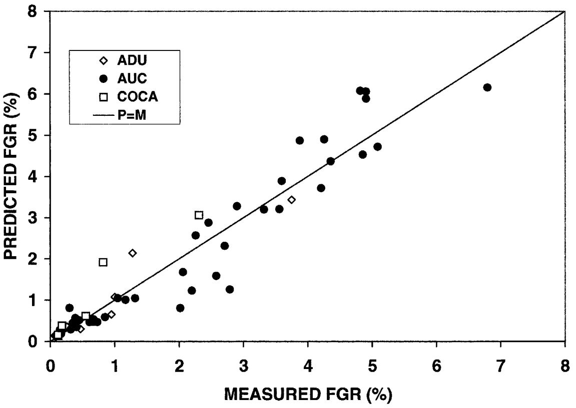

Fig. 9. Comparison between predicted and measured FGR for different MOX fuel microstructures.

tions to the FGR fraction measured in the experiment IFA-606.2-3. There is a slight over-prediction but within uncertainty bounds at the 95% level.

The transient database includes more than 60 fuel rods with burnups up to 62 GWd/tM. The transient hold times for these rods ranged from 1 min up to many hours and the LHGR ranged from 30 to 50 kW/m. Fig. 11 shows the comparison between measurements and predictions. The quality of the prediction is good, considering the wide range of conditions. Also, the upper bound for the transient model remains below of factor 2 above the best-estimate predictions, which is a good result as it is comparable to the state-of-the-art [13]. Another aspect of the quality of the transient FGR model is illustrated in Fig. 12. This figure compares predictions and measurements for the HATAC-C2 experiment [23] irradiated in the French CEA test reactor SILOE. In this experiment, a measurement device obtained on-line measurements of FGR from a 50 GWd/tM rodlet submitted to 10 successive transients. The burst effect is clearly seen on the first transient and well reproduced by the calculation.

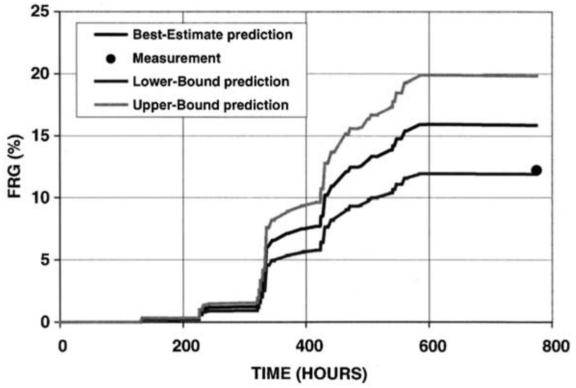

Fig. 10. FIGARO experimental program: comparison between FGR predictions and measurements for the rodlet IFA-606.2-3 irradiated at HALDEN (MOX fuel at 47 GWd/tM, peak power at 32 kW/m).

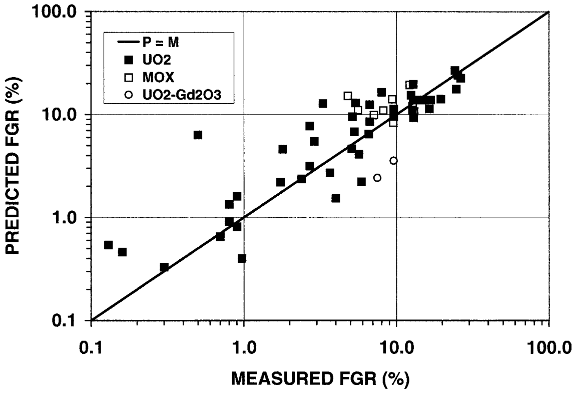

Fig. 11. Validation of the transient FGR model.

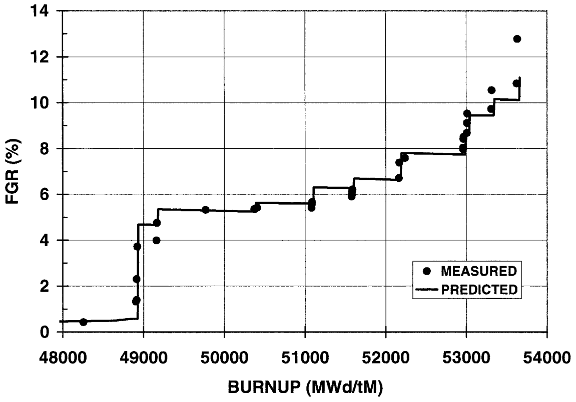

Fig. 12. HATAC-C2 experiment: rodlet irradiated at the CEA SILOE test reactor during 10 successive transients.

7. Conclusion

The Framatome ANP database and modeling of FGR are presented. They are part of COPERNIC, the Framatome ANP advanced fuel rod performance code. As FGR strongly depends upon temperature, the thermal model used and its qualification are first briefly described. Diffusion is the major FGR mechanism and a small uncertainty on temperature may yield a rather large uncertainty on the gas release fraction, as the activation energies of the diffusion coefficient are high.

The Framatome ANP FGR model reflects the industrial context of its application. It is simple as it does not require space and time integration algorithms. Thus it is efficient, fast and robust. The FGR model includes the important phenomena that contribute to FGR: athermal, thermal, steady-state and transient regimes, rim, burst effect, UO_2 and mixed oxides. It is qualified over a large database that covers the wide range of phenomena described. Overall, the quality of the prediction of the FGR model is state-of-the-art for all types of fuel rod irradiation.

There is still a need for continuing progress in FGR modeling, as new data will soon become available at high burnups and on mixed oxides. Good temperature predictions will remain a concern. Fast algorithms will remain a need in an industry framework, even more for anticipated statistical analyses that require full core calculations. In this later case, uncertainty distribution functions for the FGR model will have to be assessed.

References

[1] L.C. Bernard, E. Van Schel, V. Rebeyrolle, C. Foissaud, D. Wesley, in: International Topical Meeting in Light Water Reactor Fuel Performance, Park City, USA, 2000.

[2] K. Lassmann, H. Blank, Nucl. Eng. Des. 106 (1988) 291.

[3] L. Heins, in: Proceedings of the Top Fuel Meeting, Avignon, France, 1999, p. 451.

[4] K. Lassmann, C. O'Carroll, J. Van de Larr, in: Proceedings of the AIEA Technical Committee Meeting, Windermere, UK, 1994.

[5] L.C. Bernard, in: Annual Meeting on Nuclear Technology, Munich, Germany, 1998, p. 347.

[6] L.C. Bernard, P. Blanpain, in: Proceedings of the IAEA Technical Committee Meeting on Nuclear Fuel Behaviour Modelling at High Burnup and its Experimental Support, Windermere, UK, 2000.

[7] S. Bourreau, B. Kapusta, P. Couffin, G.M. Decroix, J.C. Couty, E. Van Schel, in: Proceedings of the Seminar on Thermal Performance of High Burnup LWR Fuel, Cadarache, France, 1998, p. 211.

[8] W. Wiesenack, in: Proceedings of the International Topical Meeting on Light Water Reactor Fuel Performance, Portland, USA, 1997, p. 507.

[9] L. Mertens, M. Lippens, J. Alvis, Report HALDEN HPR-349 Vol. II, 1998.

[10] S. Beguin, Report HALDEN HWR-603, 1999.

[11] P.G. Lucuta, Hj. Matzke, I.J. Hastings, J. Nucl. Mater. 232 (1996) 166.

[12] M.T. Alvarez, M. Hirai, W. Wiesenack, Report HALDEN HWR-470, 1996.

[13] P. Chantoin, J.A. Turnbull, W. Wiesenack, Nucl. Eng. Int. 42 (518) (1997) 32.

[14] D.R. Olander, Fundamental aspects of nuclear reactor fuel elements, ERDA, USA, 1974.

[15] D.M. Dowling, R.J. White, M.O. Tucker, J. Nucl. Mater. 110 (1982) 37.

[16] K. Forsberg, A.R. Massih, J. Nucl. Mater. 135 (1985) 140.

[17] L.C. Bernard, E. Bonnaud, J. Nucl. Mater. 244 (1997) 75.

[18] J.A. Turnbull, R.J. White, C. Wise, in: Proceedings of the IAEA Technical Committee Meeting on Water Reactor Fuel Element Computer Modelling, Preston, UK, 1988.

[19] R.J. White, Report HADLEN HWR-550, 1998.

[20] M.V. Speight, Nucl. Sci. Eng. 37 (1969) 180.

[21] C. Vitanza, E. Kolstad, U. Graziani, in: Proceedings ANS Topical Meeting in LWR Fuel Performance, Portland, OR, 1979, p. 361.

[22] A.H. Booth, Report Atomic Energy of Canada Limited CRDC-721, 1957.

[23] E. Porrot, M. Charles, J.P. Hairon, C. Lemaigan, C. Forat, M. Montagnon, in: Proceedings of the International Topical Meeting on LWR Fuel Performance, Avignon, France, Vol. 2, 1991, p. 558.